JACS
JOURNAL OF THE AMERICAN CHEMICAL SOCIETY
pubs.acs.org/JACS
Article

Solid-State End-On to Side-On Isomerization of $(N{=}N)^{2-}$ in $\{[(R_2N)_3Nd]_2N_2\}^{2-}$ (R = $SiMe_3$) Connects In Situ $Ln^{III}(NR_2)_3$/K and Isolated $[Ln^{II}(NR_2)_3]^{1-}$ Dinitrogen Reduction

Amanda B. Chung, Dmitrij Rappoport, Joseph W. Ziller, Roger E. Cramer,* Filipp Furche,* and William J. Evans*

Cite This: J. Am. Chem. Soc. 2022, 144, 17064−17074
Read Online

ABSTRACT: Examination of the reduction chemistry of Nd$(NR_2)_3$ (R = $SiMe_3$) under N_2 has provided connections between the in situ Ln(III)-based $Ln^{III}(NR_2)_3$/K reductions of N_2 that form side-on bound neutral $(N{=}N)^{2-}$ complexes, $[(R_2N)_2(THF)Ln]_2[\mu\text{-}\eta^2\text{:}\eta^2\text{-}N_2]$, and the Ln(II)-based $[Ln^{II}(NR_2)_3]^{1-}$ reductions by Sc, Gd, and Tb that form end-on bound $(N{=}N)^{2-}$ complexes, $\{[(R_2N)_3Ln]_2[\mu\text{-}\eta^1\text{:}\eta^1\text{-}N_2]\}^{2-}$, which are dianions. The reduction of $Nd(NR_2)_3$ by KC_8 under dinitrogen in Et_2O in the presence of 18-crown-6 (18-c-6) forms dark yellow solutions of $[K_2(18\text{-c-}6)_3]\{[(R_2N)_3Nd]_2N_2\}$ at low temperatures that become green as they warm up to −35 °C in a glovebox freezer. Green crystals obtained from the solution turn yellow-brown when cooled below −100 °C, and the yellow-brown compound has an end-on $Nd_2(\mu\text{-}\eta^1\text{:}\eta^1\text{-}N_2)$ structure. The yellow-brown crystals isomerize in the solid state on the diffractometer upon warming, and at −25 °C, the crystals are green and have a side-on $Nd_2(\mu\text{-}\eta^2\text{:}\eta^2\text{-}N_2)$ structure. Collection of X-ray diffraction data at 10 °C intervals from −50 to −90 °C revealed that the isomerization occurs at temperatures below −100 °C. In the presence of tetrahydrofuran (THF), the dianionic $\{[(R_2N)_3Nd]_2N_2\}^{2-}$ system can lose an amide ligand to provide the monoanionic $[(R_2N)_3Nd^{III}(\mu\text{-}\eta^2\text{:}\eta^2\text{-}N_2)Nd^{III}(NR_2)_2(THF)]^{1-}$, characterized by X-ray crystallography. These data suggest a connection between the in situ Ln(III)/K reductions and Ln(II) reductions that depends on solvent, temperature, the presence of a chelate, and the specific rare-earth metal.

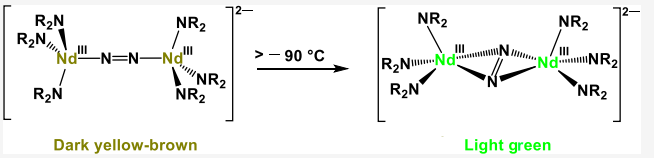

INTRODUCTION

The reduction chemistry of dinitrogen has been heavily studied for over a century due to its importance in industrial and biological processes.[1,2] A variety of binding modes have been observed for dinitrogen with transition metals,[3−9] Figure 1,[7] and interconversions between these modes can occur upon metal-based reduction or hydrogenation.[10−14] In contrast, with rare-earth metals, the side-on bridging mode was the only coordination mode for many years.

The reduction of dinitrogen by lanthanide complexes was initiated with the Sm(II) complex, $(C_5Me_5)_2Sm$, which reacted with N_2 to form $[(C_5Me_5)_2Sm]_2[\mu\text{-}\eta^2\text{:}\eta^2\text{-}N_2]$, eq 1.[15] This complex was the first isolated rare-earth metal dinitrogen complex and also the first example of planar side-on η^2-N_2 binding mode for any M_2N_2 complex of any metal.

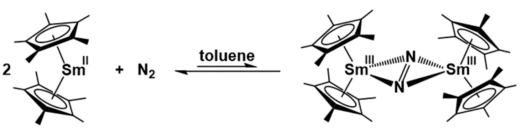

The initially unusual $M_2(\mu\text{-}\eta^2\text{:}\eta^2\text{-}N_2)$ structure defined a paradigm that became the signature structure of rare-earth metal dinitrogen complexes.[16−19] Examples with other rare-earth metals were originally generated from isolable Tm(II), Dy(II), and Nd(II) precursors, as shown in eq 2.[17−20]

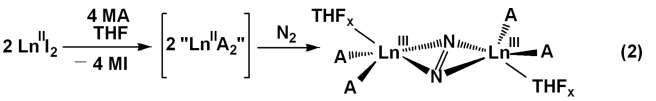

Ln = Nd, Dy, Tm
A = $N(SiMe_3)_2$, $OC_6H_3{}^tBu_2$-2,6, C_5Me_5, C_5Me_4H
M = K, KC_8, Na; x = 0-2

Subsequently, the reduced dinitrogen complexes were isolated for the whole lanthanide series through a reaction labeled LnA_3/M (A = anion; M = alkali metal), which started with Ln(III) precursors, eq 3.[21−23] Although the reaction would be expected to involve Ln(II) reactants, as in eqs 1 and 2, molecular Ln(II) complexes for many of the metals in eq 3 were unknown when this reaction was discovered.[24,25]

Received: June 26, 2022
Published: September 8, 2022

https://doi.org/10.1021/jacs.2c06716
J. Am. Chem. Soc. 2022, 144, 17064−17074

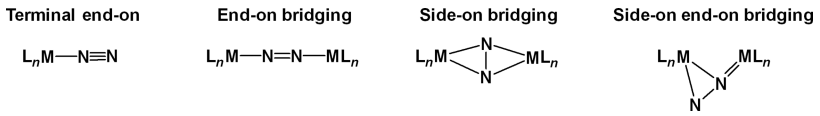

Figure 1. Some known binding modes of N_2 with transition metals.[7]

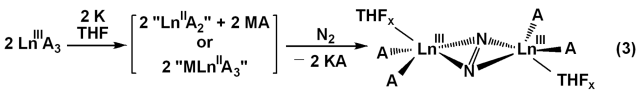

More recently, complexes of Ln(II) ions of all of the lanthanides except radioactive promethium were discovered,[24−27] which made it possible to examine the reactions of these isolated Ln(II) species with dinitrogen. Initial studies of the reactions of isolated $[Ln^{II}(NR_2)_3]^{1-}$ (R = $SiMe_3$) complexes of Ln = Sc[28] and Tb[29] revealed that these generated an M_2N_2 structural motif different from those in eqs 1−3, namely one with end-on coordination of the reduced dinitrogen, i.e., M−N=N−M, as shown in eq 4.

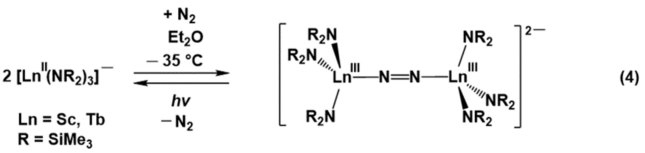

The end-on complexes differed from the neutral side-on species in that they are dianions, $\{[(R_2N)_3Ln]_2[\mu\text{-}\eta^1\text{:}\eta^1\text{-}N_2]\}^{2-}$, which have three ancillary amide ligands per metal instead of the two ancillary amide ligands per metal found in $[(THF)(R_2N)_2Ln]_2[\mu\text{-}\eta^2\text{:}\eta^2\text{-}N_2]$ (THF = tetrahydrofuran) formed via eqs 2 and 3. The reaction in eq 4 was complicated by the fact that the end-on $(N=N)^{2-}$ complexes would revert back to the Ln(II) complexes upon warming or exposure to ambient light. This reactivity was observed for both $[K(18\text{-c-}6)]^{1+}$ (18-c-6 = 18-crown-6) and $[K(crypt)]^{1+}$ (crypt = 2.2.2-cryptand) salts of $[Tb^{II}(NR_2)_3]^{1-}$ but only for the $[K(18\text{-c-}6)]^{1+}$ salt of $[Sc^{II}(NR_2)_3]^{1-}$ (see below).[28,29]

In the case of the reduction of dinitrogen by $[Gd^{II}(NR_2)_3]^{1-}$, single crystals of the product were found to be a mixture of both the end-on and side-on species, $\{[(R_2N)_3Ln]_2[\mu\text{-}\eta^x\text{:}\eta^x\text{-}N_2]\}^{2-}$, eq 5.[29] This was found to occur for both $[K(18\text{-c-}6)]^{1+}$ and $[K(crypt)]^{1+}$ salts of $[Gd^{II}(NR_2)_3]^{1-}$.

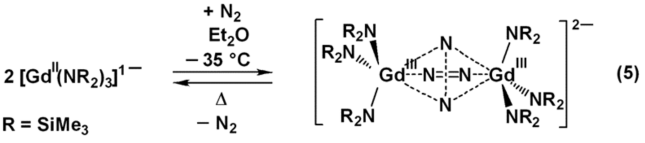

These studies indicated that the results of these dinitrogen reduction reactions were highly dependent upon specific conditions. For example, isolated $[K(crypt)][Sc(NR_2)_3]$ in THF would not reduce N_2. However, exposure of an Et_2O solution of $[K(18\text{-c-}6)_2][Sc(NR_2)_3]$ to N_2 or reduction of $Sc(NR_2)_3$ with KC_8 under a N_2 atmosphere in Et_2O in the presence of crypt gave $[(R_2N)_3Sc]_2[\mu\text{-}\eta^1\text{:}\eta^1\text{-}N_2]^{2-}$ products.[28] Both $[K(18\text{-c-}6)_2][Gd^{II}(NR_2)_3]$ and $[K(crypt)][Gd^{II}(NR_2)_3]$ reduce N_2 to afford the mixed complex in eq 5 in Et_2O. However, when the reaction is carried out in THF, the crypt Gd(II) complex gives an $(N_2)^{3-}$ product, $[K(crypt)]\{[(THF)\text{-}(R_2N)_2Gd^{III}]_2[\mu\text{-}\eta^2\text{:}\eta^2\text{-}N_2]\}$.[29]

Since the smaller metals such as Sc and Tb formed end-on $\{[(R_2N)_3Ln]_2[\mu\text{-}\eta^1\text{:}\eta^1\text{-}N_2]\}^{2-}$ complexes and the larger Gd formed a mixture of end-on and side-on species, it was of interest to look at an even larger metal to see if side-on would be favored in this series of dianions. We report here on the reduction chemistry of $Nd(NR_2)_3$ with N_2, which generates a Nd_2N_2 complex that undergoes a solid-state side-on to end-on isomerization that provides a connection between Ln(II) and $Ln^{III}A_3$/M reduction reactions.

RESULTS

Synthesis of $[K_2(18\text{-c-}6)_3][\{(R_2N)_3Nd\}_2(N_2)]$, 1-Nd. Under an atmosphere of N_2, a solution of light blue $Nd(NR_2)_3$ and 18-c-6 in Et_2O, chilled to −35 °C, was added to a vial containing excess KC_8, chilled to −116 °C. The solution became dark yellow and was filtered and placed in a −35 °C freezer. As the solution warmed to −35 °C, the solution became light green, and light green crystals were isolated after several days. As a light green crystal was cooled on the diffractometer from room temperature to −180 °C, it became yellow-brown. Data were collected on the yellow-brown crystal at −180 °C, which revealed it to be the end-on structure

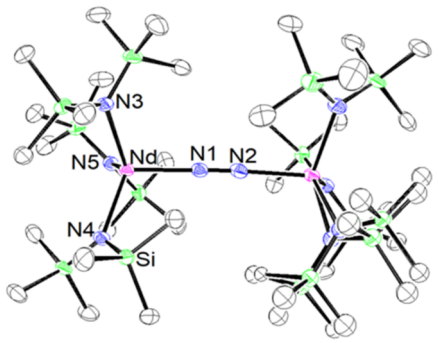

Figure 2. Representation of **1-Nd(end-on)** drawn at the 50% probability level. Hydrogen atoms, the $[K_2(18\text{-c-}6)_3]^{2+}$ countercation, and an Et_2O molecule in the lattice are not shown.

$[K_2(18\text{-c-}6)_3][\{(R_2N)_3Nd\}_2(\mu\text{-}\eta^1\text{:}\eta^1\text{-}N_2)]$, **1-Nd(end-on)**, Figure 2.

The color change of this crystal from light green to yellow-brown was observed to be reversible. When the data collection temperature was changed to −25 °C, the crystal became green again, and the X-ray data showed that it had a side-on structure, $[K_2(18\text{-c-}6)_3][\{(R_2N)_3Nd\}_2(\mu\text{-}\eta^2\text{:}\eta^2\text{-}N_2)]$, **1-Nd(side-on)**, Figure 3, eq 6. The data show that the dinitrogen unit is disordered (see below). Green crystals of **1-Nd(side-on)** also become yellow-brown when cooled to −116 °C in the cold well of the glovebox, but in the Et_2O solution, the green to dark yellow transformation is not observed.

https://doi.org/10.1021/jacs.2c06716
J. Am. Chem. Soc. 2022, 144, 17064−17074

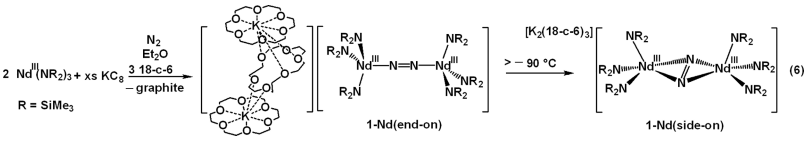

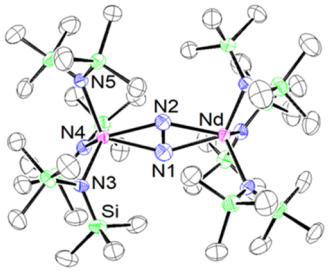

Figure 3. Representation of **1-Nd(side-on)** drawn at the 50% probability level. The N_2 unit is disordered above and below the plane made by the two Nd atoms and the average position of the nitrogen atoms, but only one form is shown here for clarity. Hydrogen atoms, the $[K_2(18\text{-c-}6)_3]^{2+}$ countercation, and an Et_2O molecule in the lattice are not shown.

Once the solid-state isomerization of **1-Nd(side-on)** to **1-Nd(end-on)** was observed, X-ray crystallographic data were collected on a single crystal at 10 °C intervals from −50 to −130 °C. It was necessary to start at the higher temperature and slowly lower the temperature because attempts to start at a low temperature and raise the temperature cracked the crystals so that useful data could not be obtained at higher temperatures. The error limits on the data did not allow detailed analysis of bond distance changes as a function of temperature, in part due to the quality of the crystal, disorder, thermal motion at higher temperatures, and degradation of the crystal during the 13-day period over which the data were collected. A concern was the choice of space groups. It was possible to solve and refine the structures in both P1 and $P\bar{1}$. Since P1 is less common for organometallic complexes, the structures were refined in $P\bar{1}$. The data sets collected at −50, −60, −70, and −80 °C showed exclusively side-on $Nd_2(\mu\text{-}\eta^2\text{:}\eta^2\text{-}N_2)$ coordination at the limits of detection. At temperatures below −100 °C, the end-on contribution was seen exclusively at the limits of detection. Between −90 and −100 °C, there was a transition from side-on to end-on coordination and the structures are likely to be mixtures of end-on and side-on like those found for gadolinium in $\{[(R_2N)_3Gd]_2[\mu\text{-}\eta^x\text{:}\eta^x\text{-}N_2]\}^{2-}$, eq 5.[29] It is difficult to specify the exact ratios of the equilibrium mixture due to the quality of the data mentioned above.

Temperature changes led to changes in the unit cell volume consistent with the isomerization analysis given above. The unit cell volume decreases with decreasing temperature from −50 °C (5942.4 Å^3) to −80 °C (5917.1 Å^3). However, in the side-on to end-on transition range, the volume increases from −90 °C (5883.2 Å^3) to −100 °C (5998.4 Å^3).

Variations in Et_2O solvent coordination were also observed as the temperature changed. At higher temperatures, from −25 to −80 °C, the Et_2O is bound to the potassium atom (K2). At −90 °C and lower temperatures, the Et_2O is not bound to the potassium. However, the Et_2O has distances consistent with hydrogen bonding between its CH_2 component and an oxygen of the crown ether. For example, the C(73B)−O(15) distance is 3.446 Å which is in the range of such interactions.[30−33]

Complex **1-Nd** is isomorphous with the previously observed $[K_2(18\text{-c-}6)_3][\{(R_2N)_3Gd\}_2(\mu\text{-}\eta^x\text{:}\eta^x\text{-}N_2)]$[29] as well as with the newly characterized $[K_2(18\text{-c-}6)_3][\{(R_2N)_3Dy\}_2(\mu\text{-}\eta^x\text{:}\eta^x\text{-}N_2)]$ (x = 1, 2) and $[K_2(18\text{-c-}6)_3][\{(R_2N)_3Y\}_2(\mu\text{-}\eta^1\text{:}\eta^1\text{-}N_2)]$ complexes described below. This system is further complicated by the fact that the oxide complex, $[K_2(18\text{-c-}6)_3]$-$[\{(R_2N)_3Nd\}_2(O)]$, is also isomorphous (see the Supporting Information, SI). An analogous oxide was also observed for Gd.[29]

Synthesis of [K(crypt)][{(THF)(R$_2$N)$_2$Nd}(N$_2$){Nd(NR$_2$)$_3$}], 2-Nd. Reactions using 2.2.2-cryptand (crypt) in eq 6 instead of 18-c-6 as the potassium chelator were also examined. Following the same procedure that generated **1-Nd**, a solution of $Nd(NR_2)_3$ and crypt in Et_2O, chilled to −35 °C, was added to a vial containing excess KC_8, chilled to −116 °C under N_2. These reactions generated yellow solutions that become green upon warming. However, crystalline products were not isolable except in one case in which the sample was exposed to THF in the glovebox. Light green crystals were characterized by X-ray crystallography to be a side-on $(N{=}N)^{2-}$ complex where one Nd center is ligated by three amides and the other is ligated by two amides and a THF molecule, $[K(crypt)][\{(THF)(R_2N)_2Nd\}(\mu\text{-}\eta^2\text{:}\eta^2\text{-}N_2)\{Nd(NR_2)_3\}]$, **2-Nd**, Figure 4, eq 7.

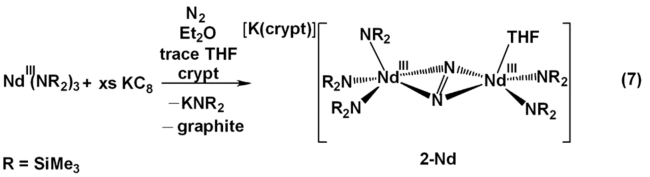

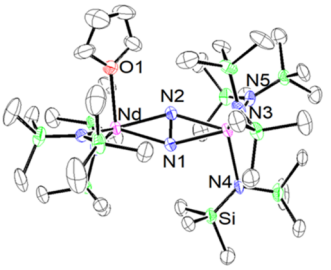

Figure 4. Representation of **2-Nd** drawn at the 50% probability level. Hydrogen atoms and the $[K(crypt)]^{1+}$ countercation are not shown.

Crystallographic Data. Crystallographic data on **1-Nd(end-on)** at −180 °C, **1-Nd(side-on)** at −25 °C, and **2-Nd** at −180 °C were compared with that of the neutral complex, $[(THF)(R_2N)_2Nd]_2(\mu\text{-}\eta^2\text{:}\eta^2\text{-}N_2)$, **3-Nd**, in Table 1, but it should be noted that the data were collected at different temperatures. The 1.205(5) Å N−N distance in **1-Nd(end-on)** is consistent with a double bond, i.e., $(N{=}N)^{2-}$.[34,35] The **1-Nd(side-on)** structure has high thermal motion in some atoms, possibly due to the high collection temperature (−25

https://doi.org/10.1021/jacs.2c06716
J. Am. Chem. Soc. 2022, 144, 17064−17074

Table 1. Selected Metrical Parameters for $[K_2(18\text{-c-}6)_3][\{(R_2N)_3Nd\}_2(\mu\text{-}\eta^x{:}\eta^x\text{-}N_2)]$, **1-Nd**, $[K(crypt)][\{(THF)(R_2N)_2Nd\}(\mu\text{-}\eta^2{:}\eta^2\text{-}N_2)\{Nd(NR_2)_3\}]$, **2-Nd**, and $[(THF)(R_2N)_2Nd]_2(\mu\text{-}\eta^2{:}\eta^2\text{-}N_2)$, **3-Nd** (Å)

	Data Collection Temp (°C)	N–N	Ln–N(N_2)	Ln–N(amide)
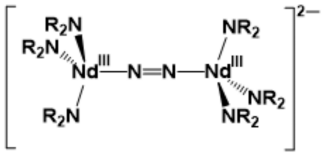 **1-Nd(end-on)**	−180	1.205(5)	2.239(4), 2.241(4)	2.389(4)–2.466(15)
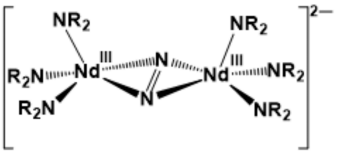 **1-Nd(side-on)**	−25 to −40	1.185(19), 1.179(18)	2.390(11)–2.441(13)	2.421(5)–2.466(5)
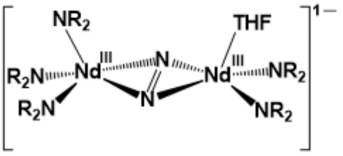 **2-Nd**	−180	1.312(6)	2.357(4)–2.425(4)	2.340(4)–2.431(4) [Ln–O: 2.528(4)]
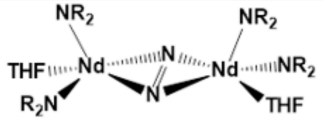 **3-Nd**	−98	1.258(3)	2.376(2)	2.328(1), 2.347(1) [Ln–O: 2.518(1)]

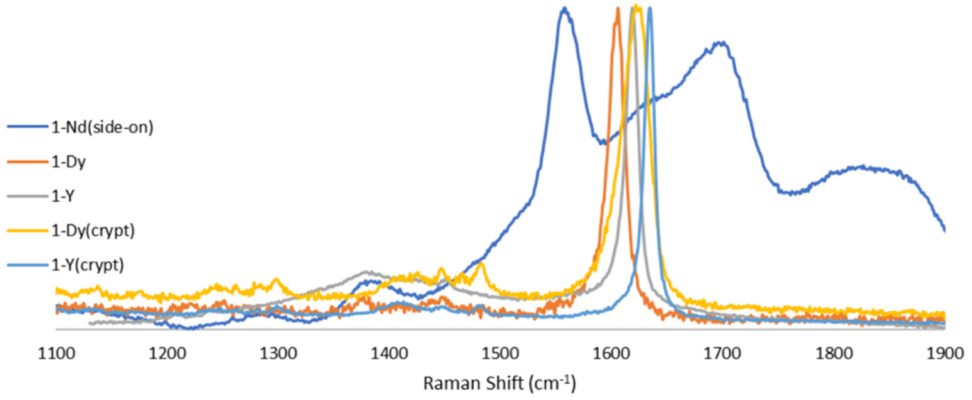

Figure 5. Normalized and baseline-corrected Raman spectra of **1-Nd(side-on)** (1557 cm^{-1}), **1-Dy** (1606 cm^{-1}), **1-Dy(crypt)** (1626 cm^{-1}), **1-Y** (1619 cm^{-1}), and **1-Y(crypt)** (1635 cm^{-1}).

°C), and the N_2 unit is disordered over two positions which average to a coplanar Nd_2N_2 unit. The N−N distances of 1.185(19) and 1.179(18) Å are equivalent within the esds of the N−N distances for **1-Nd(end-on)** and shorter than the 1.258(3) Å N−N distance of the neutral side-on bound complex, $[(THF)(R_2N)_2Nd]_2(\mu\text{-}\eta^2{:}\eta^2\text{-}N_2)$, **3-Nd**. However, the high error limits for these high-temperature data limit the usefulness of these comparisons. The 1.312(6) Å N−N distance in **2-Nd** is the longest of these distances. Comparisons with $[\{(R_2N)_3Gd\}_2(\mu\text{-}\eta^x{:}\eta^x\text{-}N_2)]^{2-}$ complexes show the variability of these distances that can occur when different chelating agents are used. For example, $[K_2(18\text{-c-}6)_3][\{(R_2N)_3Gd\}_2(\mu\text{-}\eta^x{:}\eta^x\text{-}N_2)]$, **1-Gd**, and $[K(crypt)]_2\{[(R_2N)_3Gd]_2(\mu\text{-}\eta^x{:}\eta^x\text{-}N_2)\}$, **1-Gd(crypt)**, have end-on distances of 1.234(9) and 1.271(12) Å, respectively, compared to side-on distances of 1.190(5) and 1.193(9) Å, respectively.[15] The Nd−N(N_2) distances in **1-Nd(end-on)** are significantly shorter than the analogs in **2-Nd** and **3-Nd**. This was also observed in the Gd system. The Nd−N(amide) distances in **1-Nd**, **2-Nd**, and **3-Nd** have overlapping ranges that extend from 2.328(1) to 2.467(1) Å.

Synthesis of $[\{(R_2N)_3Dy\}_2(\mu\text{-}\eta^x{:}\eta^x\text{-}N_2)]^{2-}$ and $[\{(R_2N)_3Y\}_2(\mu\text{-}\eta^1{:}\eta^1\text{-}N_2)]^{2-}$. Following the procedure in eq 6, but with Dy instead of Nd, a colorless solution of $Dy(NR_2)_3$ and 18-c-6 in Et_2O, chilled to −35 °C under an atmosphere of N_2, was added to a vial containing excess KC_8, chilled to −116

https://doi.org/10.1021/jacs.2c06716
J. Am. Chem. Soc. 2022, 144, 17064−17074

°C. The colorless solution changed to an orange solution and was filtered and placed in a −35 °C freezer. Yellow crystals were isolated after a few days and were identified by X-ray crystallography to be $[K_2(18\text{-c-}6)_3][\{(R_2N)_3Dy\}_2(\mu\text{-}\eta^x\text{:}\eta^x\text{-}N_2)]$, **1-Dy**, i.e., a two-component system as found for the dianion,$\{[(R_2N)_3Gd]_2[\mu\text{-}\eta^x\text{:}\eta^x\text{-}N_2]\}^{2-}$, in both the 18-c-6 chelated complex, **1-Gd**, and the crypt analog, **1-Gd(crypt)**. The data for **1-Dy** were modeled as a 50% end-on/50% side-on mixture.

Changing the chelate from 18-c-6 to crypt with Dy again following the same reaction in eq 6 allowed the isolation of red crystals that were identified by X-ray crystallography to be $[K(crypt)]_2[\{(R_2N)_3Dy\}_2(\mu\text{-}\eta^x\text{:}\eta^x\text{-}N_2)]$, **1-Dy(crypt)**. The data were modeled as 30% side-on and 70% end-on.

Reactions analogous to eq 6 with $Y(NR_2)_3$ generated orange crystals, which were identified as $[K_2(18\text{-c-}6)_3][\{(R_2N)_3Y\}_2(\mu\text{-}\eta^1\text{:}\eta^1\text{-}N_2)]$, **1-Y**, with 18-c-6 as the chelate and $[K(crypt)]_2[\{(R_2N)_3Y\}_2(\mu\text{-}\eta^1\text{:}\eta^1\text{-}N_2)]$, **1-Y(crypt)**, with crypt as the chelate. As indicated in the formulas, both yttrium complexes were exclusively end-on structures.

Raman Spectroscopy. Raman data were collected on crystalline samples at room temperature of $[K_2(18\text{-c-}6)_3][\{(R_2N)_3Nd\}_2(\mu\text{-}\eta^2\text{:}\eta^2\text{-}N_2)]$, **1-Nd(side-on)**, $[K_2(18\text{-c-}6)_3][\{(R_2N)_3Dy\}_2(\mu\text{-}\eta^x\text{:}\eta^x\text{-}N_2)]$, **1-Dy**, $K(crypt)_2[\{(R_2N)_3Dy\}_2(\mu\text{-}\eta^x\text{:}\eta^x\text{-}N_2)]$, **1-Dy(crypt)**, $[K_2(18\text{-c-}6)_3][\{(R_2N)_3Y\}_2(\mu\text{-}\eta^1\text{:}\eta^1\text{-}N_2)]$, **1-Y**, and $[K(crypt)]_2[\{(R_2N)_3Y\}_2(\mu\text{-}\eta^x\text{:}\eta^x\text{-}N_2)]$, **1-Y(crypt)**, Figure 5.

Strong features in the Raman spectra of **1-Dy** at 1606 cm^{-1}, **1-Dy(crypt)** at 1626 cm^{-1}, **1-Y** at 1619 cm^{-1}, and **1-Y(crypt)** at 1635 cm^{-1} were very similar to spectra obtained for **1-Sc** at 1644 cm^{-1}, **1-Tb** at 1623 cm^{-1}, and **1-Gd** at 1627 cm^{-1}, Figure 6.[28,29]

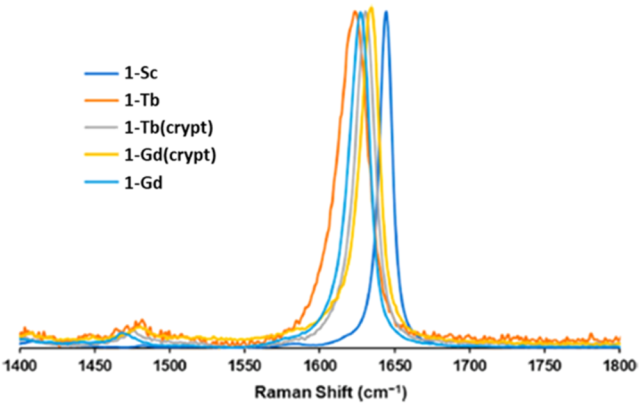

Figure 6. Normalized and baseline-corrected Raman spectra of **1-Sc** (1644 cm^{-1}), **1-Tb** (1623 cm^{-1}), **1-Tb(crypt)** (1630 cm^{-1}), **1-Gd** (1627 cm^{-1}), and **1-Gd(crypt)** (1634 cm^{-1}).[29]

Density functional theory (DFT) studies on the mixed crystal **1-Gd** indicated that the signal for end-on $(N{=}N)^{2-}$ was 2 orders of magnitude more intense than the side-on $(N{=}N)^{2-}$ stretch, which explains why only the end-on peaks are prominent in Figures 5 and 6.[29] The neutral side-on complexes, $[(R_2N)_2(THF)Ln]_2[\mu\text{-}\eta^2\text{:}\eta^2\text{-}N_2]$, **3-Ln**, have Raman features at 1413−1447 cm^{-1} for Ln = Nd, Gd, Tb, Dy, Ho, Er, and Tm.[36]

The Raman spectrum of **1-Nd** at room temperature showed a different spectrum, however, Figure 5. Since this sample should be predominantly the side-on isomer, no end-on resonance is expected. A broad absorption at 1557 cm^{-1} is observed with other bands at higher energy that could not be assigned by DFT analysis (see below).

Optical Spectroscopy. UV−visible spectra of **1-Nd** were taken at −78 °C and room temperature, Figure 7. In the room temperature spectrum of **1-Nd(side-on)**, there is one absorbance around 600 nm (ε = 180 M^{-1} cm^{-1}). This band is broader and stronger than the hypersensitive $^4I_{9/2} \rightarrow {}^4G_{5/2}$, $^2G_{7/2}$ transition, which is typical of Nd(III) complexes.[19−24] In the spectrum of **1-Nd(end-on)** at −78 °C, there is an additional absorbance at 556 nm (ε = 284 M^{-1} cm^{-1}) and a broad absorbance at 488 nm (ε = 409 M^{-1} cm^{-1}). The absorptions are analyzed by DFT as described in the next section.

Density Functional Theory. Structure optimizations were performed on the end-on and side-on $\{[(R_2N)_3Ln]_2[\mu\text{-}\eta^x\text{:}\eta^x\text{-}N_2]\}^{2-}$, for Ln = Nd, Gd, Tb, Dy, and Y by DFT using TPSSh hybrid exchange−correlation functional[37] with the Becke−Johnson dispersion correction (D3-BJ),[38,39] def2-SVP basis sets,[40,41] and the resolution-of-the-identity (RI-*J*) approximation.[42,43] In contrast to previous calculations on the Gd complexes in which large-core effective core potentials (ECPs) were used,[29] lanthanide atoms were modeled with explicit 4f orbitals and small-core ECPs.[44] The optimized structures were verified by vibrational frequency calculations. The computed harmonic frequencies were scaled by a factor of 0.97.[45]

The $\{[(R_2N)_3Nd]_2[\mu\text{-}\eta^1\text{:}\eta^1\text{-}N_2]\}^{2-}$ dianion in **1-Nd(end-on)** has an essentially linear central motif with a 1.19 Å N−N distance (exp: 1.20(1) Å at −180°C) and a 177° Nd−N−N angle. The Nd−N bonds are slightly elongated relative to the X-ray data, d(Nd−N) = 2.28 Å (exp: 2.24(1) Å at −180 °C). The Nd atoms have an approximate f^3 configuration (n/Nd = 3.24) according to the natural population analysis (NPA).[46] The analysis of the spin density on the bridging dinitrogen shows that the unpaired electrons are located in the N p-orbitals ($n_p^{spin}(N)$ = 0.54) and Nd d-orbitals ($n_d^{spin}(Nd)$ = 0.20) and constitute a triplet. The total spin expectation value $< S^2 >$ = 20.01 corresponds to a high-spin configuration with eight unpaired electrons.

The $\{[(R_2N)_3Nd]_2[\mu\text{-}\eta^2\text{:}\eta^2\text{-}N_2]\}^{2-}$ dianion in **1-Nd(side-on)** contains a planar Nd_2N_2 unit with d(N−N) = 1.24 Å (2) (exp: 1.18(2)−1.19(2) Å at −25 °C) and d(Nd−N) =2.41−2.42 Å (exp: 2.39(1)−2.43(1) Å at −25 °C). The Nd atoms have an f^3 configuration (n_f(Nd) = 3.05), while the bridging dinitrogen unit is a singlet. The spin expectation value $< S^2 >$ = 12.06 is in line with a spin septet (six unpaired electrons).

Time-dependent density functional theory (TDDFT) calculations were performed to model the UV−visible spectra. Due to reference-state instabilities in **1-Nd(end-on)** with the PBE0[47] functional, the Tamm−Dancoff Approximation (TDA) was applied,[48,49] which is more robust to instabilities. The comparison between TDA and full TDDFT results for the **1-Nd(side-on)** helps to estimate the error of TDA.

The **1-Nd(side-on)** complex is predicted by PBE0/TDA to have a prominent absorption at 543−566 nm stemming from $\pi^*(N_2) \rightarrow$ Nd f excitations, in line with the observed absorption at 600 nm, Figure 8. A weaker Nd f → f band is found at 697 nm, which is consistent with Nd(III) complexes.[50] The TDA and full TDDFT spectra are qualitatively similar for the side-on complex. However, the TDA causes the strong electronic excitations to be blue-shifted by ca. 40 nm (Figure S15 of the Supporting Information).

https://doi.org/10.1021/jacs.2c06716
J. Am. Chem. Soc. 2022, 144, 17064−17074

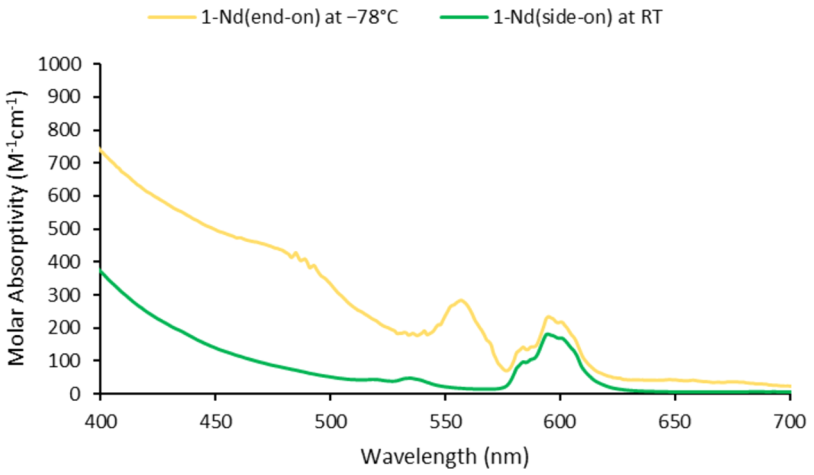

Figure 7. UV−visible absorbance spectra in Et_2O of **1-Nd(side-on)** at room temperature (green) and **1-Nd(end-on)** at −78 °C (yellow).

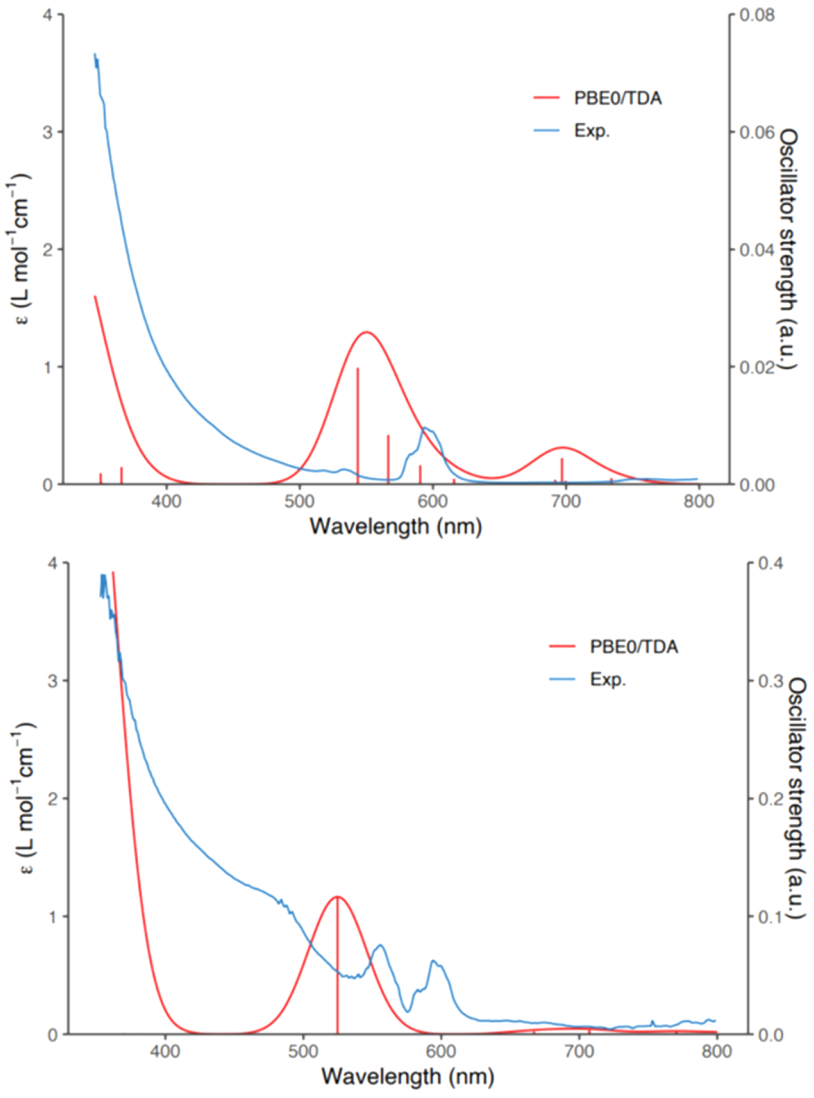

Figure 8. Predicted (red) UV−vis spectra of **1-Nd(end-on)** (top) and **1-Nd(side-on)** (bottom) overlayed on experimental (blue).

The predicted electronic absorption spectrum of the dianion in **1-Nd(end-on)**, Figure 8, also features a single strong absorption band, in this case at 525 nm, i.e., at higher energy than the **1-Nd(side-on)** prediction. The 525 nm absorption is associated with the excitation from the nearly degenerate HOMO in the complex, which has predominantly $\pi^*(N_2)$ character, into Nd f orbitals. As in **1-Nd(side-on)**, long-wavelength absorptions around 700 nm are also predicted due to the characteristic f →f transitions of Nd(III).[50]

https://doi.org/10.1021/jacs.2c06716
J. Am. Chem. Soc. 2022, 144, 17064−17074

Scheme 1. General Scheme Showing How Reduction of N_2 by LnA_3/M Reactions at Room Temperature Could Connect to Reductions With Isolated Ln(II) Complexes at Low Temperature[a]

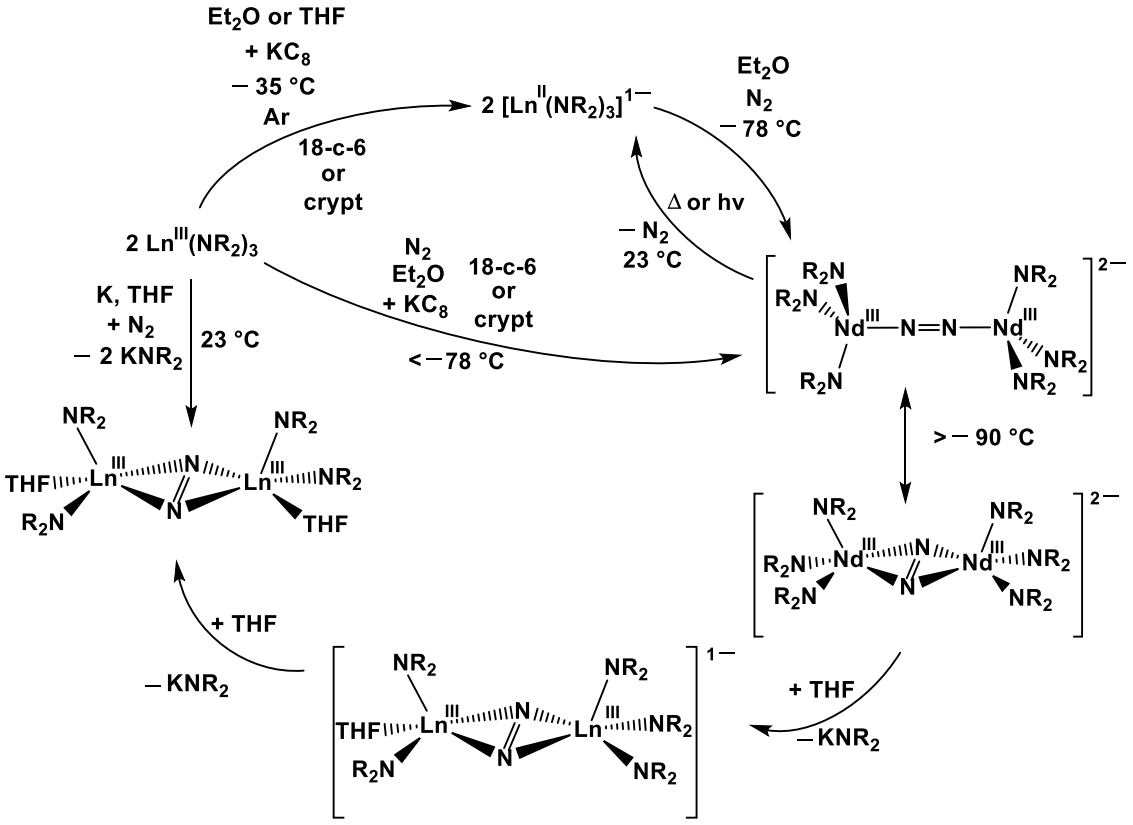

[a]Examples of all of the complexes in the scheme are known, although not every example is stable enough to be isolated with every rare-earth metal.

Experimentally, two absorptions are found in the spectrum of **1-Nd** at −78 °C. One matches that of **1-Nd(side-on)**, and the other is at higher energy as predicted by DFT for the end-on isomer. The higher energy absorption disappears within 30 s as the sample warms up (see the SI) as expected for an end-on to side-on isomerization. Hence, the −78 °C UV−vis spectrum is likely showing a mixture of the two isomers, and the spectra are in good agreement with the calculations.

Calculations on the Raman spectra also matched the experimental results. The end-on complex is predicted to have an intense stretching Raman mode at 1738 cm^{-1}. The frequency of this mode is strongly downshifted to 1562 cm^{-1} in the side-on complex due to the back-donation from the d(Nd) orbitals to the $\pi^*(N_2)$ orbitals, which leads to the weakening of the N−N bond. Vibrational frequencies are somewhat overestimated due to the small basis set size. Increasing the basis set size to def2-TZVP[40,41] for the Nd and bridging N atoms gives a vibrational frequency of 1695 cm^{-1} in the end-on complex and 1528 cm^{-1} in the side-on complex.[45] Experimental Raman data were only obtained at room temperature, so data on only the side-on isomer can be compared. The 1557 cm^{-1} resonance found for **1-Nd(side-on)** is consistent with the calculations, but the additional resonances in the spectrum, Figure 5, were not modeled by the calculations and remain puzzling since they do not seem to be due to fluorescence.

Metrical and spectral calculations on the isomers of $\{[(R_2N)_3Ln]_2[\mu\text{-}\eta^x\text{:}\eta^x\text{-}N_2]\}^{2-}$ for Ln = Gd, Tb, Dy, and Y are described in the SI. The trend in predicted Raman stretches for the side-on isomers compares well with experimental values; they are 1666, 1541, 1533, 1530, and 1528 cm^{-1} for Gd, Tb, Y, Dy, and Nd, respectively, compared to the experimental values in the same order, 1630, 1623, 1619, 1606, and 1557 cm^{-1}.

Examination of the $\{[(R_2N)_3Gd]_2[\mu\text{-}\eta^x\text{:}\eta^x\text{-}N_2]\}^{2-}$ system with an explicit treatment of the 4f orbitals revealed low-energy distorted end-on structures with the $(N{=}N)^{2-}$ group rotated relative to the Gd...Gd vector by 27°. The similarities of the energies of the end-on, side-on, and distorted end-on structures suggest that rotation of the $(N{=}N)^{2-}$ unit between the two metal centers can occur with a low energy barrier. This is consistent with the experimental data that show mixtures of structures in single crystals.

DISCUSSION

Connecting $Ln^{III}(NR_2)_3$/K and $[Ln^{II}(NR_2)_3]^{1-}$ Reductions. Examination of the reduction of $Nd(NR_2)_3$ at low temperatures in Et_2O in the presence of 18-crown-6 provides a crystal system, **1-Nd**, that demonstrates a solid-state isomerization of an end-on bound $(N{=}N)^{2-}$ moiety to the side-on structure found in most of the previously reported rare-earth metal complexes of reduced dinitrogen ligands. The results of this study provide a basis to suggest a connection between the LnA_3/M reductions of N_2 and the Ln(II) reductions, Scheme 1, which depends on temperature, solvent, and the presence of a potassium chelating agent.

The $Ln^{III}(NR_2)_3$/K reactions in the absence of N_2 and in the presence of potassium chelating agents can form isolable $[Ln^{II}(NR_2)_3]^{1-}$ compounds, which have been crystallographically characterized for Ln = Nd, Gd, Tb, Dy, Ho, Er, Y, and

https://doi.org/10.1021/jacs.2c06716
J. Am. Chem. Soc. 2022, 144, 17064−17074

Sc.[51,52] These will react with N_2 at −78 °C in the dark to form end-on dianions, $\{[(R_2N)_3Ln]_2(\mu\text{-}\eta^1\text{:}\eta^1\text{-}N_2)\}^{2-}$, which have been confirmed by X-ray diffraction for Ln = Nd, Gd, Tb, Dy, Y, Sc.[28,29] For Ln = Nd, the end-on species, observable at low temperature, can isomerize as the temperature increases to the side-on dianion, $\{[(R_2N)_3Ln]_2(\mu\text{-}\eta^2\text{:}\eta^2\text{-}N_2)\}^{2-}$, at temperatures below −90 °C as observed on the diffractometer. This is consistent with the mixed-isomer structures found for Ln = Gd and Dy.

If THF is present, it can displace an $(NR_2)^{1-}$ ligand to form a side-on monoanion, $[(R_2N)_3Ln^{III}(\mu\text{-}\eta^2\text{:}\eta^2\text{-}N_2)\text{-}Ln^{III}(NR_2)_2(THF)]^{1-}$, as has been crystallographically defined for Ln = Nd and Gd.[29] If this monoanion undergoes one more substitution of amide for THF, the neutral $[(R_2N)_2(THF)\text{-}Ln]_2[\mu\text{-}\eta^2\text{:}\eta^2\text{-}N_2]$ would result.[22] The latter complexes have been generated by $Ln(NR_2)_3$/K reactions at room temperature in THF in the absence of a potassium chelate for Ln = Nd, Gd, Tb, Dy, and Y.[22]

Hence, in the weaker donor solvent, Et_2O, at low temperature, in the dark, and with a chelate to stabilize the potassium cation, it is possible to access isolable Ln(II) complexes which reduce N_2 to end-on Ln−N═N−Ln species. The end-on dianions, $\{[(R_2N)_3Ln]_2(\mu\text{-}\eta^1\text{:}\eta^1\text{-}N_2)\}^{2-}$, are likely the first products of the reaction of $[Ln^{II}(NR_2)_3]^{1-}$ anions with N_2. Subsequent $[\mu\text{-}\eta^1\text{:}\eta^1\text{-}N_2]$ to $[\mu\text{-}\eta^2\text{:}\eta^2\text{-}N_2]$ rearrangement is evidently possible, and substitution of amide ligands by THF with reduction of an overall charge of the complex logically leads to the $[(R_2N)_2(THF)Ln]_2[\mu\text{-}\eta^2\text{:}\eta^2\text{-}N_2]$ products isolated from the room temperature reactions in THF without a chelate, Scheme 1.

End-On Versus Side-On as a Function of Metal. This study was initiated because it seemed that end-on coordination was favored by smaller rare-earth metals, e.g., Sc and Tb, and side-on by larger metals since Gd formed mixed-isomer species. The Nd result shows that the two forms are close in energy, and isomerization can occur in the solid state. The isolation of the pure end-on structures of $[K_2(18\text{-c-}6)_3]\text{-}[\{(R_2N)_3Y\}_2(\mu\text{-}\eta^1\text{:}\eta^1\text{-}N_2)]$ and $[K(crypt)]_2[\{(R_2N)_3Y\}_2(\mu\text{-}\eta^1\text{:}\eta^1\text{-}N_2)]$ fits the pattern that end-on is favored by smaller metals. However, isolation of the mixed side-on and end-on Dy complexes, $[K_2(18\text{-c-}6)_3][\{(R_2N)_3Dy\}_2(\mu\text{-}\eta^x\text{:}\eta^x\text{-}N_2)]$ and $[K(crypt)_2][\{(R_2N)_3Dy\}_2(\mu\text{-}\eta^1\text{:}\eta^1\text{-}N_2)]$, indicates that there is not a clear-cut correlation between structure and the size of the metal since Dy is smaller than Tb.

CONCLUSIONS

The $Nd(NR_2)_3/KC_8$ dinitrogen reduction system conducted in Et_2O at low temperatures in the presence of 18-crown-6 provided an ideal metal/ligand combination to elucidate the connection between end-on $\{[(R_2N)_3Ln]_2(\mu\text{-}\eta^1\text{:}\eta^1\text{-}N_2)\}^{2-}$ and side-on $\{[(R_2N)_3Ln]_2(\mu\text{-}\eta^2\text{:}\eta^2\text{-}N_2)\}^{2-}$ $(N{=}N)^{2-}$ products obtained with rare-earth metal amide complexes. Specifically, the Nd system provided single crystals that isomerize in the solid state from $\{[(R_2N)_3Nd]_2(\mu\text{-}\eta^1\text{:}\eta^1\text{-}N_2)\}^{2-}$ to $\{[(R_2N)_3Nd]_2(\mu\text{-}\eta^2\text{:}\eta^2\text{-}N_2)\}^{2-}$ at temperatures below −90 °C on the diffractometer. This provides the link which connects the $Ln(NR_2)_3/KC_8/N_2$ reactions which give the side-on $[(R_2N)_2(THF)Ln]_2[\mu\text{-}\eta^2\text{:}\eta^2\text{-}N_2]$ products at room temperature in THF to the end-on products observed from reactions at low temperatures in Et_2O in the presence of potassium chelators. The results emphasize the importance of subtle factors in controlling the reactivity of the rare-earth metal complexes and that these metals are not just simple ionic systems that behave monotonically.

EXPERIMENTAL DETAILS

All manipulations and syntheses described below were conducted with the rigorous exclusion of air and water using standard Schlenk line and glovebox techniques under an argon or dinitrogen atmosphere. Solvents were sparged with UHP argon and dried by passage through columns containing Q-5 and molecular sieves prior to use. Elemental analyses were conducted on a PerkinElmer 2400 Series II CHNS elemental analyzer. Infrared spectra were collected on an Agilent Cary 630 equipped with a diamond ATR attachment. UV−visible spectra were collected in Et_2O in a 1 mm cell fitted with a Teflon stopcock using an Agilent Cary 60 UV−visible spectrophotometer. Raman spectra were collected on solid samples in a 1 mm quartz cuvette appended with a Teflon stopcock using a Renishaw inVia confocal Raman Microscope, equipped with a 122 mW laser of wavelength 785 nm (laser power 10% and an XSL objective laser). Measurements were taken on at least three different crystals to confirm reproducibility. 2.2.2-Cryptand (crypt, Merck) was placed under vacuum (10^{-4} torr) for 12 h before use. 18-Crown-6 (18-c-6, Alfa Aesar) was sublimed before use. $Nd(NR_2)_3$, $Dy(NR_2)_3$, and $Y(NR_2)_3$ were synthesized according to literature procedures.[53]

$[K_2(18\text{-c-}6)_3]\{[(NR_2)_3Nd]_2[\mu\text{-}\eta^1\text{:}\eta^1\text{-}N_2]\}$, 1-Nd(end-on), and $[K_2(18\text{-c-}6)_3]\{[(NR_2)_3Nd]_2[\mu\text{-}\eta^2\text{:}\eta^2\text{-}N_2]\}$, 1-Nd(side-on). In a dinitrogen-filled glovebox, $Nd(NR_2)_3$ (50 mg, 0.080 mmol) and 18-crown-6 (32 mg, 0.12 mmol) were dissolved in chilled (−35 °C), nitrogen-saturated Et_2O (2 mL) and placed in a −35 °C freezer for 1 h. This light blue solution was then added to a vial containing excess KC_8 (24 mg, 0.18 mmol) at −116 °C. The solution was immediately filtered and placed in a −35 °C freezer. As the resulting dark yellow solution warmed to this temperature, it became light green color from which bright green crystals of **1-Nd(side-on)** (34 mg, 38%) suitable for X-ray diffraction were grown. Under the cold stream of the diffractometer (−180 °C), the light green crystals turned to a yellow-brown color of **1-Nd(end-on)**. **1-Nd(side-on)** IR (cm^{-1}): 2994m, 2888m, 1470w, 1453w, 1352s, 1240s, 1107s, 985m, 945s, 862m, 823s, 765m, 699w, 659m. **1-Nd(side-on)** UV−vis in Et_2O: λ_{max} = 600 nm (ε = 180 M^{-1} cm^{-1}). **1-Nd(end-on)** UV−vis in Et_2O: λ_{max} = 556 nm (ε = 284 M^{-1} cm^{-1}) and 488 nm (ε = 409 M^{-1} cm^{-1}). **1-Nd(side-on)** anal. calcd for $C_{70}H_{190}N_8O_{19}Si_{12}K_2Nd_2$: C, 41.81; H, 8.77; N, 4.88. Found: C, 41.67; H, 8.71; N, 3.87. Multiple samples gave low nitrogen values, and it is possible that N_2 is lost before combustion is complete.

$[K(crypt)]\{[(THF)(R_2N)_2Nd][\mu\text{-}\eta^2\text{:}\eta^2\text{-}N_2][Nd(NR_2)_3]\}$ 2-Nd. In a dinitrogen-filled glovebox, $Nd(NR_2)_3$ (50 mg, 0.08 mmol) and 2.2.2-cryptand (30 mg, 0.08 mmol) were dissolved in chilled (−35 °C), nitrogen-saturated Et_2O (2 mL) and placed in a −35 °C freezer for 1 h. This light blue solution was then added to a vial containing excess KC_8 (24 mg, 0.18 mmol) at −116 °C. The solution was immediately filtered and placed in a −35 °C freezer overnight. The solution was exposed to trace THF that was present in the box. Bright green crystals of **2-Nd** suitable for X-ray diffraction studies were grown from the resulting green solution. Subsequent attempts to deliberately synthesize this complex to obtain more characterization data were unsuccessful.

$[K_2(18\text{-c-}6)_3]\{[(NR_2)_3Dy]_2[\mu\text{-}\eta^x\text{:}\eta^x\text{-}N_2]\}$, 1-Dy. In a dinitrogen-filled glovebox, $Dy(NR_2)_3$ (50 mg, 0.078 mmol) and 18-crown-6 (31 mg, 0.12 mmol) were dissolved in −35 °C, nitrogen-saturated, Et_2O (2 mL) and placed in a −35 °C freezer for 1 h. This colorless solution was then added to a vial containing excess KC_8 (24 mg, 0.18 mmol) at −116 °C. The solution was immediately filtered and placed in a −35 °C freezer. The resulting dark yellow/orange solution produced yellow crystals of **1-Dy** (23 mg, 26%) suitable for X-ray diffraction. IR (cm^{-1}): 2944w, 2887w, 1473w, 1452w, 1352w, 1237m, 1104m, 943m, 868m, 814m, 770w, 756w, 704w, 652m. UV−vis in Et_2O: λ_{max} = 360 nm.

$[K(crypt)]_2\{[(NR_2)_3Dy]_2[\mu\text{-}\eta^x\text{:}\eta^x\text{-}N_2]\}$, 1-Dy(crypt). In a dinitrogen-filled glovebox, $Dy(NR_2)_3$ (50 mg, 0.078 mmol) and crypt (29

https://doi.org/10.1021/jacs.2c06716
J. Am. Chem. Soc. 2022, 144, 17064−17074

mg, 0.078 mmol) were dissolved in chilled (−35 °C), nitrogen-saturated, Et_2O (2 mL) and placed in a −35 °C freezer for 1 h. This colorless solution was then added to a vial containing excess KC_8 (24 mg, 0.18 mmol) at −116 °C. The solution was immediately filtered and placed in a −35 °C freezer. Red crystals of **1-Dy(crypt)** (27 mg, 32%) that were suitable for X-ray diffraction studies were grown from the resulting yellow/orange solution. IR (cm^{-1}): 2944w, 2884w, 2818w, 1479w, 1445w, 1354w, 1223m, 1132w, 1101m, 943m, 868m, 814m, 770w, 753w, 702w, 652m.

$[K_2(18\text{-c-}6)_3]\{[(NR_2)_3Y]_2[\mu\text{-}\eta^1\text{:}\eta^1\text{-}N_2]\}$, 1-Y. In a dinitrogen-filled glovebox, $Y(NR_2)_3$ (50 mg, 0.088 mmol) and 18-crown-6 (35 mg, 0.13 mmol) were dissolved in chilled (−35 °C), nitrogen-saturated, Et_2O (2 mL) and placed in a −35 °C freezer for 1 h. This colorless solution was then added to a vial containing excess KC_8 (27 mg, 0.20 mmol) at −116 °C. The orange solution was immediately filtered and placed in a −35 °C freezer. Orange crystals of **1-Y** (16 mg, 17%) suitable for X-ray diffraction studies were grown from the resulting yellow/orange solution. IR (cm^{-1}): 2944w, 2888w, 1470w, 1452w, 1352w, 1237m, 1104m, 945m, 865m, 815m, 773w, 750w, 702w, 654m. UV−vis in Et_2O: λ_{max} = 357 nm (ε = 383 M^{-1} cm^{-1}).

$[K(crypt)]_2\{[(NR_2)_3Y]_2[\mu\text{-}\eta^1\text{:}\eta^1\text{-}N_2]\}$, 1-Y(crypt). In a dinitrogen-filled glovebox, $Y(NR_2)_3$ (50 mg, 0.088 mmol) and crypt (33 mg, 0.088 mmol) were dissolved in chilled (−35 °C), nitrogen-saturated, Et_2O (2 mL) and placed in a −35 °C freezer for 1 h. This colorless solution was then added to a vial containing excess KC_8 (27 mg, 0.20 mmol) at −116 °C. The solution was immediately filtered and placed in a −35 °C freezer. Orange crystals of **1-Y(crypt)** (17 mg, 19%) suitable for X-ray diffraction studies were grown from the resulting yellow/orange solution. IR (cm^{-1}): 2948w, 2889w, 1476w, 1442w, 1353w, 1298w, 1240m, 1137w, 1103w, 1107m, 962w, 948w, 925w, 865w, 823m, 770w, 753w, 702w, 665w. UV−vis in Et_2O: λ_{max} = 362 nm.

Computational Methods. Structure optimizations of the end-on and side-on dianions, $\{[(R_2N)_3Ln]_2[\mu\text{-}\eta^x\text{:}\eta^x\text{-}N_2]\}^{2-}$, were performed for Ln = Nd, Gd, Tb, Dy, and Y. The initial structures of the **1-Nd** and **2-Nd** complexes were extracted from X-ray data of the $[K(18\text{-crown-}6)_2]^+$ complexes. For the **1-Gd** and **2-Gd** complexes, the X-ray structure of the $[K(18\text{-crown-}6)_2]^+$ complex[29] was used as a starting point for the structure optimizations. The structure optimizations of **1-Tb** and **1-Dy** compounds were based on the X-ray structure of the $[K(crypt)]^+$ **1-Tb** complex.[29] Additionally, **2-Tb** and **2-Dy** structures were derived from the Gd analog. The structural parameters of the **1-Sc** complex were used as the initial guess for the structure optimizations of the **1-Y** complex.[28] The end-on complexes were initially treated in D_3 point group symmetry, which was lowered if necessary (see details below). The side-on complexes were assumed to have C_2 symmetry.

Structure optimizations were performed by density functional theory (DFT) with TPSSh hybrid exchange−correlation functional[37] with the Becke−Johnson dispersion correction (D3-BJ)[38,39] and the resolution-of-the-identity (RI-*J*) approximation.[42,43] def2-SVP basis sets were used for nonhydrogen atoms and def2-SV(P) for hydrogens[40,41] together with small-core relativistic effective core potentials (ECPs) of Dolg and co-workers for the lanthanide atoms.[44] Additional calculations were performed with the larger def2-TZVP basis sets for the lanthanide and bridging N atoms.[40,41] The solvation effects were treated by the conductor-like solvation model (COSMO)[54] using the experimental dielectric constant ε_r = 7.52 and the optical index of refraction n = 1.4050 of THF. The optimized structures were confirmed as stable by numerical force constant calculations. Thermodynamic functions were computed in quasi-rigid-rotor−harmonic-oscillator (qRRHO) approximation, in which the contributions from low-frequency vibrations are treated as free rotors.[55] Harmonic vibrational frequencies were scaled down using a global factor of 0.97.[45]

Raman spectra of the **1-Nd** and **2-Nd** complexes were computed using vibrational frequencies from TPSSh calculations and static polarizability derivatives[56] using the PBE0 functional,[47] def2-SVP basis sets, and the COSMO solvation model for THF. Harmonic vibrational frequencies were scaled by an empirical factor of 0.97[45] to account for anharmonicity and broadened using Gaussian profiles with an empirical line width of 20 cm^{-1}.

UV−visible absorption spectra of the optimized **1-Nd** and **2-Nd** complexes were simulated by time-dependent density functional theory (TDDFT) using the PBE0 hybrid functional, def2-SVP basis sets, the RI-*J* approximation, and the COSMO solvation model as in the ground-state calculations. Due to ground-state instabilities, TDDFT calculations using the Tamm-Dancoff approximation (TDA)[48,49] were additionally performed for both complexes **1-Nd** and **2-Nd**. The computed spectra were broadened using Gaussian profiles with an empirical full width at half maximum (FWHM) parameter of 50 nm.

X-ray Crystallographic Data. Crystallographic information for the complexes is summarized in the Supporting Information.

■ ASSOCIATED CONTENT

Supporting Information

The Supporting Information is available free of charge at https://pubs.acs.org/doi/10.1021/jacs.2c06716.

Spectroscopic research and crystallographic information (PDF)

Video of the isomerization of **1-Nd** (AVI)

Accession Codes

CCDC 2180561−2180571 contain the supplementary crystallographic data for this paper. These data can be obtained free of charge via www.ccdc.cam.ac.uk/data_request/cif, or by emailing data_request@ccdc.cam.ac.uk, or by contacting The Cambridge Crystallographic Data Centre, 12 Union Road, Cambridge CB2 1EZ, UK; fax: +44 1223 336033.

■ AUTHOR INFORMATION

Corresponding Authors

Roger E. Cramer − *Department of Chemistry, University of Hawaii, Manoa, Honolulu, Hawaii 96822-2275, United States;* orcid.org/0000-0002-3934-3401; Email: rcramer@hawaii.edu

Filipp Furche − *Department of Chemistry, University of California, Irvine, California 92697-2025, United States;* orcid.org/0000-0001-8520-3971; Email: filipp.furche@uci.edu

William J. Evans − *Department of Chemistry, University of California, Irvine, California 92697-2025, United States;* orcid.org/0000-0002-0651-418X; Email: wevans@uci.edu

Authors

Amanda B. Chung − *Department of Chemistry, University of California, Irvine, California 92697-2025, United States;* orcid.org/0000-0001-8943-0303

Dmitrij Rappoport − *Department of Chemistry, University of California, Irvine, California 92697-2025, United States;* orcid.org/0000-0002-5024-7998

Joseph W. Ziller − *Department of Chemistry, University of California, Irvine, California 92697-2025, United States;* orcid.org/0000-0001-7404-950X

Complete contact information is available at: https://pubs.acs.org/10.1021/jacs.2c06716

Notes

The authors declare the following competing financial interest(s): Principal Investigator Filipp Furche has an equity interest in TURBOMOLE GmbH. The terms of this arrangement have been reviewed and approved by the

University of California, Irvine, in accordance with its conflict of interest policies.

■ ACKNOWLEDGMENTS

The authors thank the U.S. National Science Foundation (CHE-2154255 to W.J.E. and CHE-2102568 to F.F.) for support and Austin J. Ryan for the X-ray crystal structure of **1-Dy(crypt)**.

■ REFERENCES

(1) Burford, R. J.; Fryzuk, M. D. Examining the Relationship between Coordination Mode and Reactivity of Dinitrogen. *Nat. Rev. Chem.* **2017**, *1*, 1−13.
(2) Tanabe, Y. Group 3 Transition Metal, Lanthanide, and Actinide−Dinitrogen Complexes. In *Transition Metal-Dinitrogen Complexes: Preparation and Reactivity*; Wiley, 2019; pp 441−474.
(3) Leigh, G. J. Protonation of Coordinated Dinitrogen. *Acc. Chem. Res.* **1992**, *25*, 177−181.
(4) Harrison, D. F.; Weissberger, E.; Taube, H. Binuclear Ion Containing Nitrogen as a Bridging Group. *Science* **1968**, *159*, 320−322.
(5) Chatt, J.; Dilworth, J. R.; Leigh, G. J.; Richards, R. L. Polynuclear Dinitrogen Complexes. *J. Chem. Soc. D* **1970**, *15*, 955−956.
(6) Fryzuk, M. D.; Haddad, T. S.; Mylvaganam, M.; McConville, D. H.; Rettig, S. J. End-On Versus Side-On Bonding of Dinitrogen to Dinuclear Early Transition-Metal Complexes. *J. Am. Chem. Soc.* **1993**, *115*, 2782−2792.
(7) Fryzuk, M. D. Side-on End-on Bound Dinitrogen: An Activated Bonding Mode That Facilitates Functionalizing Molecular Nitrogen. *Acc. Chem. Res.* **2009**, *42*, 127−133.
(8) Murray, L. J.; Weare, W. W.; Shearer, J.; Mitchell, A. D.; Abboud, K. A. Isolation of a (Dinitrogen)Tricopper(I) Complex. *J. Am. Chem. Soc.* **2014**, *136*, 13502−13505.
(9) Pun, D.; Lobkovsky, E.; Chirik, P. J. Indenyl Zirconium Dinitrogen Chemistry: N_2 Coordination to an Isolated Zirconium Sandwich and Synthesis of Side-on, End-on Dinitrogen Compounds. *J. Am. Chem. Soc.* **2008**, *130*, 6047−6054.
(10) Bernskoetter, W. H.; Lobkovsky, E.; Chirik, P. J. Kinetics and Mechanism of N_2 Hydrogenation in Bis(Cyclopentadienyl) Zirconium Complexes and Dinitrogen Functionalization by 1,2-Addition of a Saturated C-H Bond. *J. Am. Chem. Soc.* **2005**, *127*, 14051−14061.
(11) Pun, D.; Bradley, C. A.; Lobkovsky, E.; Keresztes, I.; Chirik, P. J. N_2 Hydrogenation from Activated End-on Bis(Indenyl) Zirconium Dinitrogen Complexes. *J. Am. Chem. Soc.* **2008**, *130*, 14046−14047.
(12) Semproni, S. P.; Knobloch, D. J.; Milsmann, C.; Chirik, P. J. Redox-Induced N_2 Hapticity Switching in Zirconocene Dinitrogen Complexes. *Angew. Chem., Int. Ed.* **2013**, *52*, 5372−5376.
(13) Fontaine, P. P.; Yonke, B. L.; Zavalij, P. Y.; Sita, L. R. Dinitrogen Complexation and Extent of N-N Activation within the Group 6 "End-On-Bridged" Dinuclear Complexes, $\{(\eta^5\text{-}C_5Me_5)M[N(i\text{-}Pr)C(Me)N(i\text{-}Pr)]\}_2(\mu\text{-}\eta^1\text{:}\ \eta^1\text{-}N_2)$ (M = Mo and W). *J. Am. Chem. Soc.* **2010**, *132*, 12273−12285.
(14) Keane, A. J.; Yonke, B. L.; Hirotsu, M.; Zavalij, P. Y.; Sita, L. R. Fine-Tuning the Energy Barrier for Metal-Mediated Dinitrogen N≡N Bond Cleavage. *J. Am. Chem. Soc.* **2014**, *136*, 9906−9909.
(15) Evans, W. J.; Ulibarri, T. A.; Ziller, J. W. Isolation and X-Ray Crystal Structure of the First Dinitrogen Complex of an f-Element Metal, $[(C_5Me_5)_2Sm]_2N_2$. *J. Am. Chem. Soc.* **1988**, *110*, 6877−6879.
(16) Evans, W. J.; Lee, D. S. Early Developments in Lanthanide-Based Dinitrogen Reduction Chemistry. *Can. J. Chem.* **2005**, *83*, 375−384.
(17) Evans, W. J.; Allen, N. T.; Ziller, J. W. Facile Dinitrogen Reduction via Organometallic Tm(II) Chemistry. *J. Am. Chem. Soc.* **2001**, *123*, 7927−7928.
(18) Evans, W. J.; Allen, N. T.; Ziller, J. W. Expanding Divalent Organolanthanide Chemistry: The First Organothulium(II) Complex and the in Situ Organodysprosium(II) Reduction of Dinitrogen. *Angew. Chem., Int. Ed.* **2002**, *41*, 359−361.
(19) Evans, W. J.; Zucchi, G.; Ziller, J. W. Dinitrogen Reduction by Tm (II), Dy (II), and Nd (II) with Simple Amide and Aryloxide Ligands. *J. Am. Chem. Soc.* **2003**, *125*, 10−11.
(20) Jaroschik, F.; Momin, A.; Nief, F.; Goff, X.; Le; Deacon, G. B.; Junk, P. C. Dinitrogen Reduction and C-H Activation by the Divalent Organoneodymium Complex $[C_5H_2tBu_3)_2Nd(\mu\text{-}I)K([18]Crown\text{-}6]$. *Angew. Chem., Int. Ed.* **2009**, *48*, 1117−1121.
(21) Evans, W. J.; Lee, D. S.; Ziller, J. W. Reduction of Dinitrogen to Planar Bimetallic $M_2(\mu\text{-}\eta^2\text{:}\eta^2\text{-}N_2)$ Complexes of Y, Ho, Tm, and Lu Using the $KLn[N(SiMe_3)_2]_3$ Reduction System. *J. Am. Chem. Soc.* **2004**, *126*, 454−455.
(22) Evans, W. J.; Lee, D. S.; Rego, D. B.; Perotti, J. M.; Kozimor, S. A.; Moore, E. K.; Ziller, J. W. Expanding Dinitrogen Reduction Chemistry to Trivalent Lanthanides via the LnZ_3/Alkali Metal Reduction System: Evaluation of the Generality of Forming $Ln_2(\mu\text{-}\eta^2\text{:}\eta^{\ 2}\text{-}N_2)$. *J. Am. Chem. Soc.* **2004**, *126*, 14574−14582.
(23) Evans, W. J.; Lee, D. S.; Lie, C.; Ziller, J. W. Expanding the LnZ_3/Alkali-Metal Reduction System to Organometallic and Heteroleptic Precursors: Formation of Dinitrogen Derivatives of Lanthanum. *Angew. Chem., Int. Ed.* **2004**, *43*, 5517−5519.
(24) Evans, W. J. Tutorial on the Role of Cyclopentadienyl Ligands in the Discovery of Molecular Complexes of the Rare-Earth and Actinide Metals in New Oxidation States. *Organometallics* **2016**, *35*, 3088−3100.
(25) Woen, D. H.; Evans, W. J. Expanding the +2 Oxidation State of the Rare-Earth Metals, Uranium, and Thorium in Molecular Complexes. In *Handbook on the Physics and Chemistry of Rare Earths*; Elsevier B.V, 2016; pp 1−57.
(26) Hitchcock, P. B.; Lappert, M. F.; Maron, L.; Protchenko, A. V. Lanthanum Does Form Stable Molecular Compounds in the +2 Oxidation State. *Angew. Chem., Int. Ed.* **2008**, *47*, 1488−1491.
(27) Macdonald, M. R.; Bates, E.; Ziller, J. W.; Furche, F.; Evans, W. J. Completing the Series of +2 Ions for the Lanthanide Elements: Synthesis of Molecular Complexes of Pr^{2+}, Gd^{2+}, Tb^{2+}, and Lu^{2+}. *J. Am. Chem. Soc.* **2013**, *135*, 9857−9868.
(28) Woen, D. H.; Chen, G. P.; Ziller, J. W.; Boyle, T. J.; Furche, F.; Evans, W. J. End-On Bridging Dinitrogen Complex of Scandium. *J. Am. Chem. Soc.* **2017**, *139*, 14861−14864.
(29) Ryan, A. J.; Balasubramani, S. G.; Ziller, J. W.; Furche, F.; Evans, W. J. Formation of the End-on Bound Lanthanide Dinitrogen Complexes $[(R_2N)_3Ln{-}N{=}N{-}Ln(NR_2)_3]^{2-}$ from Divalent $[(R_2N)_3Ln]^{1-}$ Salts (R = $SiMe_3$). *J. Am. Chem. Soc.* **2020**, *142*, 9302−9313.
(30) Cramer, R. E.; Rimsza, J. M.; Boyle, T. J. Structural and Computational Examination of Hydrogen-Bonding between the C-H Bonds of Phenylphosphates and Nitrate Ions. *J. Mol. Struct.* **2021**, *1242*, No. 130661.
(31) Steed, J. W.; Junk, P. C. Stabilisation of Sodium Complexes of 18-Crown-6 by Intramolecular Hydrogen Bonding. *J. Chem. Soc., Dalton Trans.* **1999**, 2141−2146.
(32) Ando, I. Hydrogen Bonding of 18-Crown-6 Ether to Ruthenium-Ammine Complexes at Second Sphere. *Coord. Chem. Rev.* **2004**, *248*, 185−203.
(33) Desiraju, G. R. The C-H···O Hydrogen Bond: Structural Implications and Supramolecular Design. *Acc. Chem. Res.* **1996**, *29*, 441−449.
(34) Allen, F. H.; Kennard, O.; Watson, D. G.; Brammer, L.; Orpen, A. G.; Taylor, R. Tables of Bond Lengths Determined by X-Ray and Neutron Diffraction. Part 1. Bond Lengths in Organic Compounds. *J. Chem. Soc., Perkin Trans. 2* **1987**, 1−19.
(35) Holland, P. L. Metal-Dioxygen and Metal-Dinitrogen Complexes: Where Are the Electrons? *Dalton Trans.* **2010**, *39*, 5415−5425.
(36) Fieser, M. E.; Woen, D. H.; Corbey, J. F.; Mueller, T. J.; Ziller, J. W.; Evans, W. J. Raman Spectroscopy of the N-N Bond in Rare Earth Dinitrogen Complexes. *Dalton Trans.* **2016**, *45*, 14634−14644.
(37) Staroverov, V. N.; Scuseria, G. E.; Tao, J.; Perdew, J. P. Comparative Assessment of a New Nonempirical Density Functional:

https://doi.org/10.1021/jacs.2c06716
J. Am. Chem. Soc. 2022, 144, 17064−17074

Molecules and Hydrogen-Bonded Complexes. *J. Chem. Phys.* **2003**, *119*, 12129−12137.
(38) Grimme, S.; Antony, J.; Ehrlich, S.; Krieg, H. A Consistent and Accurate Ab Initio Parametrization of Density Functional Dispersion Correction (DFT-D) for the 94 Elements H-Pu. *J. Chem. Phys.* **2010**, *132*, No. 154104.
(39) Grimme, S.; Ehrlich, S.; Goerigk, L. Effect of the Damping Function in Dispersion Corrected Density Functional Theory. *J. Comput. Chem.* **2011**, *32*, 1456−1465.
(40) Weigend, F.; Ahlrichs, R. Balanced Basis Sets of Split Valence, Triple Zeta Valence and Quadruple Zeta Valence Quality for H to Rn: Design and Assessment of Accuracy. *Phys. Chem. Chem. Phys.* **2005**, *7*, 3297−3305.
(41) Gulde, R.; Pollak, P.; Weigend, F. Error-Balanced Segmented Contracted Basis Sets of Double-ζ to Quadruple-ζ Valence Quality for the Lanthanides. *J. Chem. Theory Comput.* **2012**, *8*, 4062−4068.
(42) Eichkorn, K.; Treutler, O.; Öhm, H.; Häser, M.; Ahlrichs, R. Auxiliary Basis Sets to Approximate Coulomb Potentials. *Chem. Phys. Lett.* **1995**, *240*, 283−290.
(43) Bauernschmitt, R.; Häser, M.; Treutler, O.; Ahlrichs, R. Calculation of Excitation Energies within Time-Dependent Density Functional Theory Using Auxiliary Basis Set Expansions. *Chem. Phys. Lett.* **1997**, *264*, 573−578.
(44) Dolg, M.; Stoll, H.; Preuss, H. Energy-Adjusted *ab initio* Pseudopotentials for the Rare Earth Elements. *J. Chem. Phys.* **1989**, *90*, 1730−1734.
(45) Kashinski, D. O.; Chase, G. M.; Nelson, R. G.; Di Nallo, O. E.; Scales, A. N.; Vanderley, D. L.; Byrd, E. F. C. Harmonic Vibrational Frequencies: Approximate Global Scaling Factors for TPSS, M06, and M11 Functional Families Using Several Common Basis Sets. *J. Phys. Chem. A* **2017**, *121*, 2265−2273.
(46) Reed, A. E.; Weinstock, R. B.; Weinhold, F. Natural Population Analysis. *J. Chem. Phys.* **1985**, *83*, 735−746.
(47) Perdew, J. P.; Ernzerhof, M.; Burke, K. Rationale for Mixing Exact Exchange with Density Functional Approximations. *J. Chem. Phys.* **1996**, *105*, 9982−9985.
(48) Tamm, I. Relativistic Interaction of Elementary Particles. *J. Phys. USSR* **1945**, *9*, 449−460.
(49) Dancoff, S. M. Non-Adiabatic Meson Theory of Nuclear Forces. *Phys. Rev.* **1950**, *78*, 382−385.
(50) Karraker, D. G. The Hypersensitive Transitions of Hydrated Nd^{3+}, Ho^{3+}, and Er^{3+} Ions. *Inorg. Chem.* **1968**, *7*, 473−479.
(51) Ryan, A. J.; Darago, L. E.; Balasubramani, G.; Chen, G. P.; Ziller, J. W.; Furche, F.; Long, J. R.; Evans, W. J. Synthesis, Structure, and Magnetism of Tris(Amide) Lanthanide Ions. *Chem. - Eur. J.* **2018**, *24*, 7702−7709.
(52) Woen, D. H.; Chen, G. P.; Ziller, J. W.; Boyle, T. J.; Furche, F.; Evans, W. J. Solution Synthesis, Structure, and CO_2 Reduction Reactivity of a Scandium(II) Complex, $[Sc(N(SiMe_3)_2]_3]^-$. *Angew. Chem., Int. Ed.* **2017**, *129*, 2082−2085.
(53) Aspinall, H. C.; Bradley, D. C.; Hursthouse, M. B.; Sales, K. D.; Walker, N. P. C.; Hussain, B. Preparation of the Bis(trimethylsilyl)-amido Lanthanide Chlorides $[\{Ln[N(SiMe_3)_2]_2(\mu\text{-}Cl)(thf)\}_2]$ (thf = tetrahydrofuran), and the Crystal and Molecular Structures of the Gadolinium and Ytterbium Complexes. *J. Chem. Soc., Dalton Trans.* **1989**, *1*, 623−626.
(54) Klamt, A.; Schüürmann, G. COSMO: A New Approach to Dielectric Screening in Solvents with Explicit Expressions for the Screening Energy and Its Gradient. *J. Chem. Soc., Perkin Trans. 2* **1993**, *5*, 799−805.
(55) Grimme, S. Supramolecular Binding Thermodynamics by Dispersion-Corrected Density Functional Theory. *Chem. - Eur. J.* **2012**, *18*, 9955−9964.
(56) Rappoport, D.; Furche, F. Lagrangian Approach to Molecular Vibrational Raman Intensities Using Time-Dependent Hybrid Density Functional Theory. *J. Chem. Phys.* **2007**, *126*, No. 201104.

https://doi.org/10.1021/jacs.2c06716
J. Am. Chem. Soc. 2022, 144, 17064−17074